Pulse-to-Pulse Coherent Doppler Measurements of Waves and Turbulence

FABRICE VERON AND W. KENDALL MELVILLE

Scripps Institution of Oceanography, University of California, San Diego, La Jolla, California

(Manuscript received 7 August 1997, in final form 12 September 1998)

ABSTRACT

This paper presents laboratory and field testing of a pulse-to-pulse coherent acoustic Doppler profiler for the measurement of turbulence in the ocean. In the laboratory, velocities and wavenumber spectra collected from Doppler and digital particle image velocimeter measurements compare very well. Turbulent velocities are obtained by identifying and filtering out deep water gravity waves in Fourier space and inverting the result. Spectra of the velocity profiles then reveal the presence of an inertial subrange in the turbulence generated by unsteady breaking waves. In the field, comparison of the profiler velocity records with a single-point current measurement is satisfactory. Again wavenumber spectra are directly measured and exhibit an approximate $-5/3$ slope. It is concluded that the instrument is capable of directly resolving the wavenumber spectral levels in the inertial subrange under breaking waves, and therefore is capable of measuring dissipation and other turbulence parameters in the upper mixed layer or surface-wave zone.

1. Introduction

The surface-wave zone or upper surface mixed layer of the ocean has received considerable attention in recent years. This is partly a result of the realization that wave breaking (Thorpe 1993; Melville 1994; Anis and Moum 1995) and perhaps Langmuir circulations (Skyllingstad and Denbo 1995; McWilliams et al. 1997; Melville et al. 1998) may lead to enhanced dissipation and significant departures from the classical ''law-of-the-wall'' description of the surface layer (Craig and Banner 1994; Terray et al. 1996; Agrawal et al. 1992). The classical description would lead to the dissipation, ε, being proportional to z^{-1}, where z is the depth from the surface, whereas recent observations show $\varepsilon \propto z^{-2}$ to z^{-4} (Gargett 1989; Drennan et al. 1992), or $\varepsilon \propto e^{-z}$ (Anis and Moum 1995), with values of the dimensionless dissipation $\varepsilon\kappa z/u_{*_w}^3$ (where κ is the von Kármán constant and u_{*_w} the friction velocity in water) up to two orders of magnitude higher than the $O(1)$ expected for the law of the wall (Melville 1996).

Measuring the dissipation in the surface wave zone is made difficult by the wave motion, the relatively small thickness of the layer, and the general difficulty of making measurements near the air–sea interface. If breaking is the source of the high dissipation events, then the intermittency of breaking can have a significant influence on the measurement technique. For example, profiling instruments have been very successful in measuring microstructure at greater depth (Oakey and Elliot 1982; Gregg et al. 1993), but unless the turnaround time of the profiler is small compared to the time between events, the probability of sampling an intermittent event may be significantly reduced when compared with an instrument at a fixed depth. This may be difficult to achieve in the upper mixed layer. On the other hand, ''fixed'' instruments need to be mounted either on a moving buoy or vessel (Osborn et al. 1992; Drennan et al. 1996), and then the problem of transforming from a temporal signal to a spatial signal through some form of Taylor's hypothesis can be difficult if not impossible.

From the work of Agrawal et al. (1992) and the modeling of Melville (1994), we assume that the maximum dissipation rate in the wave zone will be approximately $\varepsilon = Au_{*_w}^3/\kappa z$, where to be specific we take the numerical factor to be $A = 100$. Now if we assume that U_{10} is in the range 3–15 m s^{-1} and z is in the range 1–10 m, then with the further assumption that the air–sea drag coefficient $C_D = O(10^{-3})$ (Komen et al. 1994), we find that ε ranges from 10^{-3} m^2 s^{-3} (for $z = 1$ m and $U_{10} = 15$ m s^{-1}) to 9×10^{-7} m^2 s^{-3} (for $z = 10$ m and $U_{10} = 3$ m s^{-1}). For these values of ε the Kolmogorov length η, time t_k, and velocity scales v, are (in SI units) (1.7×10^{-4}, 3×10^{-2}, 6×10^{-3}) and (10^{-3}, 1, 10^{-3}), respectively. At large Reynolds numbers the $k^{-5/3}$ subrange begins to roll off in the dissipation region at $k\eta = 0.1$. For example, for a turbulent Reynolds number $R_t = ul\nu^{-1}$ of 2×10^5, corresponding to a breaking wave of 2-s period (Rapp and Melville 1990), where u

Corresponding author address: Prof. W. Kendall Melville, Scripps Institution of Oceanography, University of California, San Diego, La Jolla, CA 92093-0213.
E-mail: kmelville@ucsd.edu

and l are, respectively, the velocity and length scales of the energy containing eddies and ν the kinematic viscosity of water, this subrange extends for two decades to lower wavenumbers before rolling off in the energy-containing range. For this particular conservative R_t we expect to have an inertial subrange over two decades of wavenumbers. Thus, for the largest ε given above we would have an inertial subrange over length scales from 0.01 to 1 m, and for the smallest ε, 0.06–6 m. In summary, for breaking-induced near-surface turbulence we expect to have inertial subranges for scales in the range O(0.01–1 m).

Since dissipation estimates are made from measurements over the inertial or dissipation subranges of the turbulent scales, it would be desirable to avoid any form of Taylor hypothesis and have an instrument that could make direct spatial (wavenumber) measurements over these ranges in the field. To our knowledge, the only means of making dense spatial measurements of velocities are either optical or acoustical. Experience in the laboratory with laser Doppler velocimetry (Rapp and Melville 1990) and a digital particle imaging velocimeter (DPIV) (Melville et al. 1998) led us to believe that optical techniques, while very attractive, may be less robust than acoustical systems in the active wave zone of the ocean. Accordingly, we decided to pursue acoustical techniques.

This paper describes our laboratory and field tests of the suitability of a pulse-to-pulse coherent acoustic Doppler instrument (Dopbeam, Sontek, San Diego) for measuring turbulence in the inertial subrange under breaking waves. Direct comparisons are made with a DPIV system in the laboratory, and with a single-point acoustic velocimeter in the field.

2. Instrumentation

a. Coherent Doppler sonar

As opposed to conventional incoherent Doppler systems, which extract the velocity from the frequency shift in the backscatter, coherent Doppler sonars transmit a series of short pulses, allowing continuous recording of the fluid velocity at densely spaced range bins. This leads to the possibility of acquiring information on the fluid turbulence (Lhermitte and Lemmin 1990, 1994; Lohrmann et al. 1990; Gargett 1994).

For each pulse, the backscattered signal is range gated. The radial velocities V are extracted using the pulse-pair coherent technique (Miller and Rochwarger 1972) by taking the time rate of change of the phase Ψ of the complex signal autocorrelation $X(\tau) = S(t)S^*(t + \tau)$. Hence

$$V = \frac{1}{2\pi}\frac{\lambda}{2}\frac{\Psi}{\tau}, \tag{1}$$

with

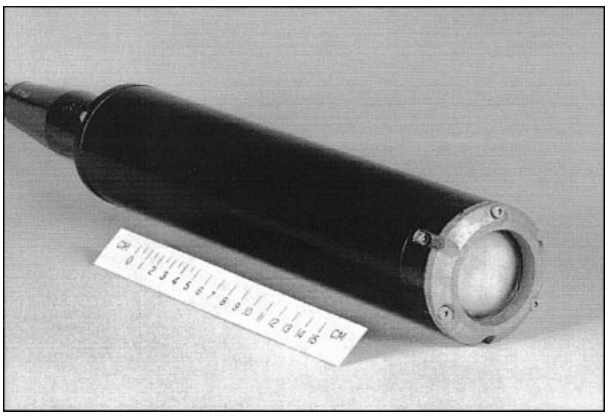

FIG. 1. Photograph of the Dopbeam head, which includes transducer and analog electronics.

$$\Psi = \tan^{-1}\left[\frac{Q(t)I(t + \tau) - I(t)Q(t + \tau)}{I(t)I(t + \tau) + Q(t)Q(t + \tau)}\right], \tag{2}$$

where λ is the system wavelength, τ is the delay between adjacent pulses, and $Q(t)$ and $I(t)$ are, respectively, the quadrature and in-phase components of the received signal $S(t)$, and $S^*(t)$ denotes the complex conjugate. Clearly, the direct velocity measurement is limited to $|\Psi| \leq \pi$, giving a maximum velocity range of

$$V_{\max} = \pm\frac{\lambda}{4\tau}. \tag{3}$$

The maximum achievable range is

$$R_{\max} = \frac{c\tau}{2}, \tag{4}$$

where c is velocity of sound in water. This leads to the well-known ''range–velocity'' ambiguity

$$R_{\max}V_{\max} = \pm\frac{\lambda c}{8}. \tag{5}$$

The Dopbeam is a 1.72-MHz, programmable, monostatic, single-beam sonar system performing pulse-to-pulse coherent Doppler measurements of the along-beam fluid velocity. Typically, it operates in the range 0.5–5 m with a direct unambiguous velocity measurement between 0.3 and 0.03 m s^{-1}. The waterproof unit is 40 cm long and 6 cm in diameter (Fig. 1). It is equipped with a single 2.5-cm-diameter transducer at one end, and an underwater connector for communication with a controller at the other end. For a circular piston transducer, the directivity of the emitted acoustic intensity is given by the Rayleigh function

$$\mathrm{Ra}(\theta) = \frac{2J_1(\pi D \sin\theta/\lambda)}{\pi D \sin\theta/\lambda}, \tag{6}$$

where J_1 is the first-order cylindrical Bessel function and D the diameter of the transducer. The spreading angle of the main lobe is then given by $\mathrm{Ra}(\theta_0) = 0$,

which leads to $\theta_0 = 2.4°$, and the half-power beam angle is given by $20 \log_{10}[\mathrm{Ra}(\theta_{3dB})] = -3$, which leads to $\theta_{3dB} = 1°$. The Fresnel zone (near field) boundary is located at $D^2/4\lambda = 18$ cm from the transducer.

b. Digital particle image velocimeter

A DPIV is a system that measures two components of velocity in a plane by measuring particle displacements between sequential images. The fluid is seeded with small, neutrally buoyant particles and illuminated with a pulsed laser light sheet. The velocity of the particles is assumed to be an accurate representation of the fluid velocity. In our case, a 5-W argon-ion laser (American Laser Cooperation Model 909, Salt Lake City, Utah) was used to illuminate a vertical sheet of particle-containing fluid along the centerline of the tank and aligned with the Doppler beam. Images are acquired by a CCD video camera (Texas Instruments TI1134P/GN) and stored on laser-video disk (Sony laser video LVR5000A) for later processing. Each frame is 480 × 768 pixels, and each pixel is assigned an 8-bit intensity level. Thus an image can be represented as a gray-level matrix $A(m, n)$. Displacements between two images (or two pulses of the laser sheet) are obtained via a two-dimensional cross correlation performed on subwindows of the images. This can be written as

$$H(m, n) = \sum_{k=-\infty}^{\infty} \sum_{l=-\infty}^{\infty} A(k + m, l + n)B(k, l), \quad (7)$$

where A and B are, respectively, the first and second subwindows of the image pair. Subwindows are 16 × 16 pixels and adjacent windows linearly overlap by 50%. The new matrix H contains a pattern of gray levels, and the center of the highest peak relative to the center of the window gives the pixel shift required for the best particle match. Finally, knowing the time delay between the two images allows the velocity to be retrieved. Note that this system does not track individual particles but gives an average fluid motion (or particle motion) for the entire subwindow.

3. Laboratory measurements

a. Calibration

Prior to the experiments, the Dopbeam was independently calibrated in the tow tank facility at the Memorial University of Newfoundland, Newfoundland, Canada, under similar conditions to those used by Zedel and his colleagues (Zedel et al. 1996). The Doppler was mounted on a cart and towed at a controlled speed along the 65-m-long channel with the beam oriented in two different directions: 80° and 40° from the direction of motion. Figure 2 shows the velocity recorded by the Dopbeam versus the tow cart velocity projected on a frame of reference aligned with the beam of the Doppler. The velocity plotted is the result of an average over 20 bins and over 5 s of data. The error bars are the standard deviation of the cart velocity. For the Dopbeam, the errors were within the symbol width. The linear fit to the data has a slope of 1.003 ± 0.001. These results are consistent with the analysis of Zedel et al. (1996) regarding the ability of the Dopbeam to measure absolute current speeds.

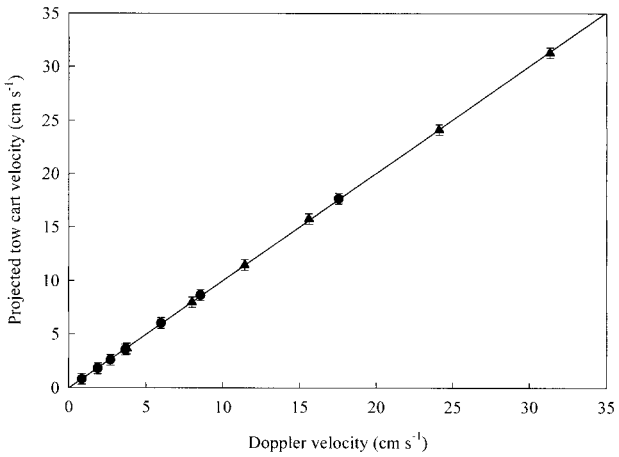

FIG. 2. Doppler velocity vs the projected cart velocity in the frame of reference relative to the Dopbeam. Doppler velocities were measured for two directions of the beam relative to the mean flow: ▲ = 40° and ● = 80°. The error bars are the standard deviation of the cart velocity. Errors for the Doppler are within the width of the symbols. The solid line is the linear fit to the data with a slope of 1.003 ± 0.001.

b. Experimental setup

The experiments were performed in the 28.7-m-long glass-walled wave channel at the Scripps Institution of Oceanography. The tank is 0.5 m wide and was filled with freshwater to a depth of 0.6 m. Waves were generated by a hydraulic paddle that sent a packet of high-frequency waves followed by low-frequency waves so that constructive interference led to breaking at a time t_b at a predetermined location x_b along the channel (see Rapp and Melville 1990; Loewen and Melville 1991). In these experiments each packet had a central frequency of $f_c = 0.99$ Hz, and consisted of 32 wave components of constant slope ak, where a is the component amplitude and k its wavenumber. Note that for a center frequency of 0.99 Hz, the phase speed and wavelength are $C_c = 1.55$ m s^{-1} and $\lambda_c = 1.57$ m, respectively. These are deep water waves, although the length of the wave group is significantly greater than the water depth. For a given central frequency and bandwidth the governing parameter is the slope $S = 32Gak$, where G is a gain parameter. The three breaking wave cases studied here are for $S = 0.608$, 0.656, and 0.704, corresponding, respectively, to a weak spiller, a strong spiller, and a weak plunger. Eight repeats for each breaking case were performed with a 15-minute time delay between events to allow for decay of any residual fluid velocities.

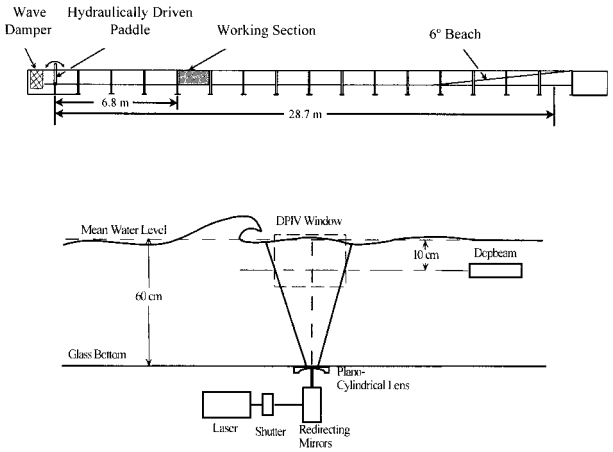

FIG. 3. Wave channel at the Hydraulics Laboratory at Scripps Institution of Oceanography, and experimental setup in the working section (not to scale).

The Dopbeam was placed 10 cm below the mean water level, facing upstream (Fig. 3). It was set to ping with a 420-Hz repetition rate. This gave a maximum unambiguous velocity of 9.16 cm s^{-1} and a maximum range of 178.5 cm. Each ping was 9.3 μs in duration, which corresponds to ensonifying a 6.9-mm-long sample volume. After a ping was transmitted, the transducer switched to receive mode and recorded the backscatter signal every 14 μs (i.e., every 1.05 cm along the 178.5-cm-long range) before transmitting another ping. This gave 170 range bins. Since the same transducer is used for transmitting and receiving, there is a ''shadow'' zone of about 10 cm in front of the transducer that corresponds to the time necessary for the electronics to switch from transmitting to receiving. Finally, for each bin, the velocity was calculated by averaging 28 successive transmissions so that the final profiling rate was 15 Hz, the same as the DPIV. For each breaking event, data were taken for 120 s, starting 2 s before the observed breaking time t_b.

The DPIV sampled a 23.6 cm $\times$ 14.6 cm window. The upstream edge of the window was located 30 cm downstream of the breaker location x_b, while the upper edge of the window was located 1 cm above the mean water level (Fig. 3). The sampling rate of the DPIV system is limited by the frame rate of the camera, namely, 30 frames per second, giving a 15-Hz sampling rate (two images for each velocity estimate). The laser was pulsed so that two consecutive fields would be separated by 20 ms. With such a configuration, the DPIV provided a grid of 91 $\times$ 56 velocity estimates in a vertical plane with a spatial resolution of 0.26 cm. Two adjacent velocities are not independent due to the overlapping subwindows, and thus the true resolution of the DPIV is 0.52 cm. The velocity fields were computed with the software package developed by Willert and Gharib (1991). With the present configuration the error on the velocities is less than 1 mm s^{-1}. Only the horizontal component of the velocity at 10-cm depth was kept for direct comparison with the Doppler data. However, the DPIV provides a two-dimensional velocity field and thus has the capability to examine the structure of the turbulence in more detail. One minute of simultaneous coincident measurements with the Dopbeam was recorded.

To ensure sufficient scatterers, the water was seeded with nearly neutrally buoyant Pliolite particles (Goodyear Chemical, Oakland, California) with a diameter $d = 100$–150 μm and a density $\rho_p = 1.024$. These particles were used both as DPIV particles and scatters for the Dopbeam. We used 0.5 kg of Pliolite to seed a volume of approximately 1 m^3. Although Doppler velocity estimates are not directly dependent on the backscattered signal amplitude, but rather the phase [Eqs. (1) and (2)], sufficient backscatter levels are required to accurately measure the phase. The acoustic backscatter amplitude is at maximum when the dimensionless size parameter $s_p = \pi d\lambda^{-1}$ approaches unity (Hay 1991; Richard et al. 1996). Here, we have s_p in the range of 0.36–0.53. Note that the characteristic response time of the particles in Stokes flow is

$$T_p = \frac{d^2}{36\nu}\left(1 + 2\frac{\rho_p}{\rho_w}\right) \tag{8}$$

and ranges from 0.85 to 1.9 ms, where ρ_w is the density of water. As a consequence, the characteristic timescales of the particles are much smaller than the expected Kolmogorov timescales. This ensures that the particles will accurately follow the turbulent fluid motion. Moreover, given the sampling rate and sampling volume of both instruments, we are confident that the Pliolite particles, although not strictly spherical, will follow the fluid motion up to scales and frequencies beyond the measurement capabilities of both instruments (Snyder and Lumley 1971; Seigel and Plueddemann 1991).

c. Results

Figure 4a shows a typical breaking event ($S = 0.656$) measured with the Dopbeam and the DPIV. It shows the along-beam velocity as a function of time and range, with the vertical axis being the time from breaking and the horizontal axis the downstream distance from the observed breaker position x_b. Immediately following the breaking event, velocity levels were too high to be directly resolved by either of the two instruments and therefore the data presented here start 4 s after the breaker. Bubble entrainment may also cause difficulties immediately after breaking. However, at a depth of 10 cm and after four wave periods, the volume fraction of air, or void fraction in the water, is then dramatically reduced to approximately 10^{-6}, with the largest bubbles still in solution having radii between 200 and 300 μm (Terrill 1998; Terrill and Melville 2000). The velocity is given by the color code with positive velocities toward the Dopbeam (or downstream) denoted by a red shift.

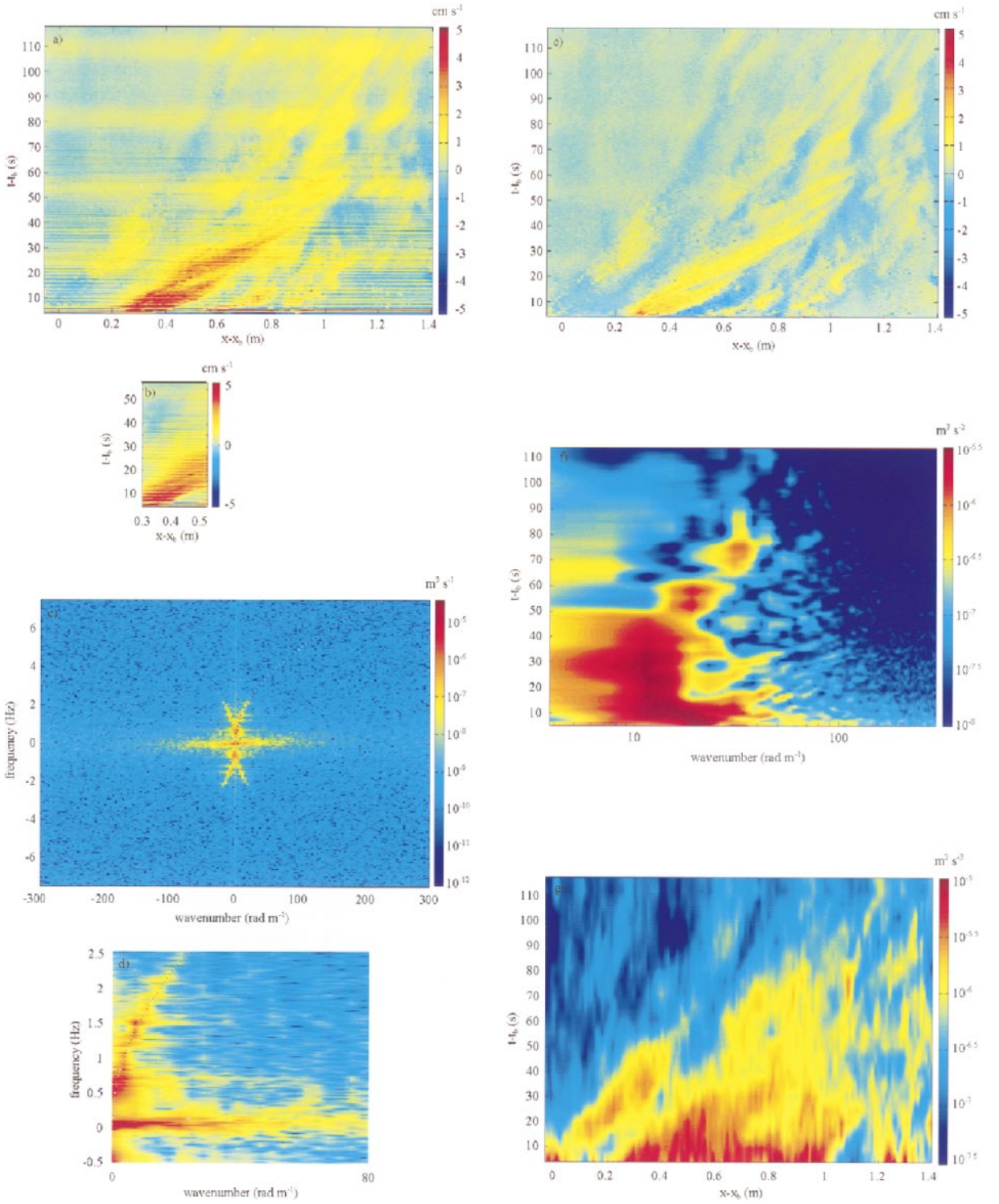

FIG. 4. Example of velocity data recorded by (a) the Dopbeam and (b) the DPIV for a breaker with a slope of $S = 0.656$. The horizontal axis represents the downstream distance from the location of the breaker x_b, and the vertical axis is the time elapsed from t_b, the time of the breaking event. (c) Wavenumber–frequency spectrum of the data from (a). The dash line is the linear dispersion relationship for deep water gravity waves. (d) A close-up of (c) plotted for frequencies between -0.5 and 2.5 Hz and wavenumbers ranging from 0 to 80 rad m^{-1}. (e) Velocity corresponding to the data of (a) with the surface waves filtered out. (f) Wavenumber spectrogram calculated from the data of (e). (g) Estimate of the kinetic energy dissipation $\varepsilon(x, t)$ using Eq. (20) and the data of (e). The data shown have a resolution of 5 s in time and 1.05 cm in range. For clarity, the data have been linearly interpolated in the time domain. Note the fast decay and the intermittency of the shear beneath the breaker.

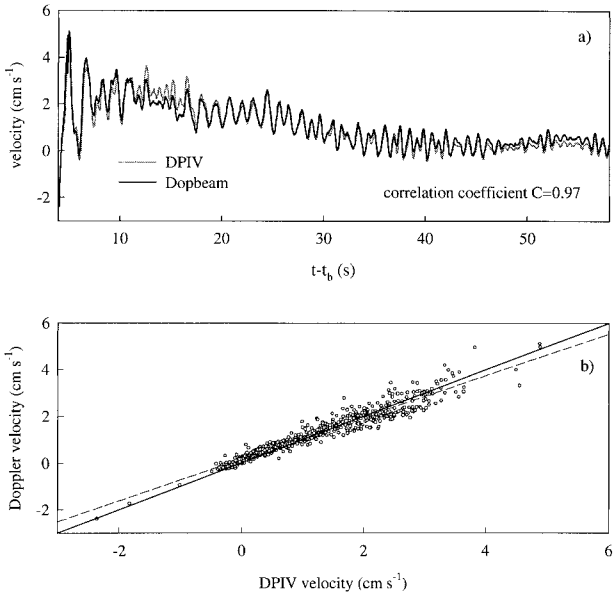

FIG. 5. (a) Comparison of simultaneous velocity time series recorded by the Dopbeam and the DPIV. The velocities are range averaged over the common profile. (b) Doppler velocity vs DPIV velocity. The solid line has a slope of unity. The dashed line is the linear fit to the data and has a slope of 0.89.

1) MEASUREMENT CONSISTENCY CHECKS

Despite the limited spatial range of the DPIV system, when compared with the Dopbeam, examination of Figs. 4a and 4b show that the two instruments agree qualitatively with similar features observed in both records. In both figures, the nearly horizontal lines are fast surface waves. Note that Fig. 4a shows surface waves traveling both upstream and downstream, as well as a weak seiche of approximately 28-s period excited by the breaker and appearing with peaks around 25, 55, 82, and 110 s. The alternating bands of positive and negative velocities are vortices, generated by the breaking, slowly moving downstream. The agreement between instruments is also verified by plotting a time series of the range-averaged velocity measured by both instruments (Fig. 5a). For this comparison, the DPIV velocity field was averaged over the vertical region sampled by the Dopbeam. Then, both datasets were range averaged over the common 23.6-cm-long profile. Since the Dopbeam samples over the axisymmetric acoustic beam and the DPIV samples over a plane, this comparison is not exact; nevertheless, Fig. 5 shows good agreement between the two simultaneous sets of measurements. The velocity records are correlated at 97%.

It is also possible to check the quality of the Doppler velocity estimate by calculating the correlation coefficient associated with each velocity,

$$C = \frac{|X(\tau)|}{|S(t)||S(t+\tau)|}, \tag{9}$$

where $S(t)$ is the complex received signal, $X(\tau)$ the complex signal autocorrelation, and the vertical bars indicate that the modulus of the value is kept. This coefficient ranges from 0 to 1 and represents the correlation between two successive pings, or the quality of the received signal. It is thus a measure of the quality of the velocity estimate from the pair of pings. Assuming a Gaussian-shaped frequency spectrum of the transmitted signal, the correlation coefficient can be related to the Doppler frequency variance σ_f^2 (Lhermitte and Serafin 1984):

$$C = \exp[-2\pi^2\sigma_f^2\tau^2]. \tag{10}$$

Since the velocity variance σ_u^2 for a single pair of pings is also a function of the Doppler frequency variance,

$$\sigma_f = \frac{2\sigma_u}{\lambda}, \tag{11}$$

the velocity uncertainty is directly related to the correlation coefficient by

$$C = \exp\left[\frac{-8\pi^2\sigma_u^2\tau^2}{\lambda^2}\right]. \tag{12}$$

Figure 6a shows the plot of correlation coefficients corresponding to the data in Fig. 4a and Fig. 6b is the profile-averaged time series of C. The slightly reduced correlation just after the breaker is likely due to high velocity, high void fraction, and cross-beam motion [for a discussion on decorrelation processes, see Cabrera et al. (1987) and Zedel et al. (1996)]. The overall average correlation coefficient for the event is $\langle\overline{C}\rangle = 0.96$, where the overbar represents the averaging in time and the angle brackets, averaging in space. Such a correlation coefficient yields a Doppler velocity error of 8.3 mm s^{-1}, which reduces to 1.6 mm s^{-1} when averaged over 28 consecutive transmissions.

2) TURBULENCE

From Fig. 4a, it appears that most of the velocity field can be identified as either orbital motion due to surface waves or turbulence. Indeed, performing a two-dimensional spectrum of the velocity field in space and time confirms this interpretation.

The wavenumber–frequency spectrum (Fig. 4c) of the data of Fig. 4a clearly shows the deep-water waves in the neighborhood of the dispersion curve. Note that in Fig. 4c, quadrants 1 and 2 are symmetric with quadrants 3 and 4, respectively. Quadrant 1 (positive wavenumber and positive frequency) corresponds to downstream propagation, and quadrant 2 (negative wavenumber and positive frequency) corresponds to upstream propagation. Both positive and negative phase velocities are apparent, corresponding to waves traveling downstream and upstream, respectively. As expected, the upstream traveling waves (reflected waves) are weaker than those traveling downstream. From the exponential decay of orbital velocities with depth for deep-water waves, we

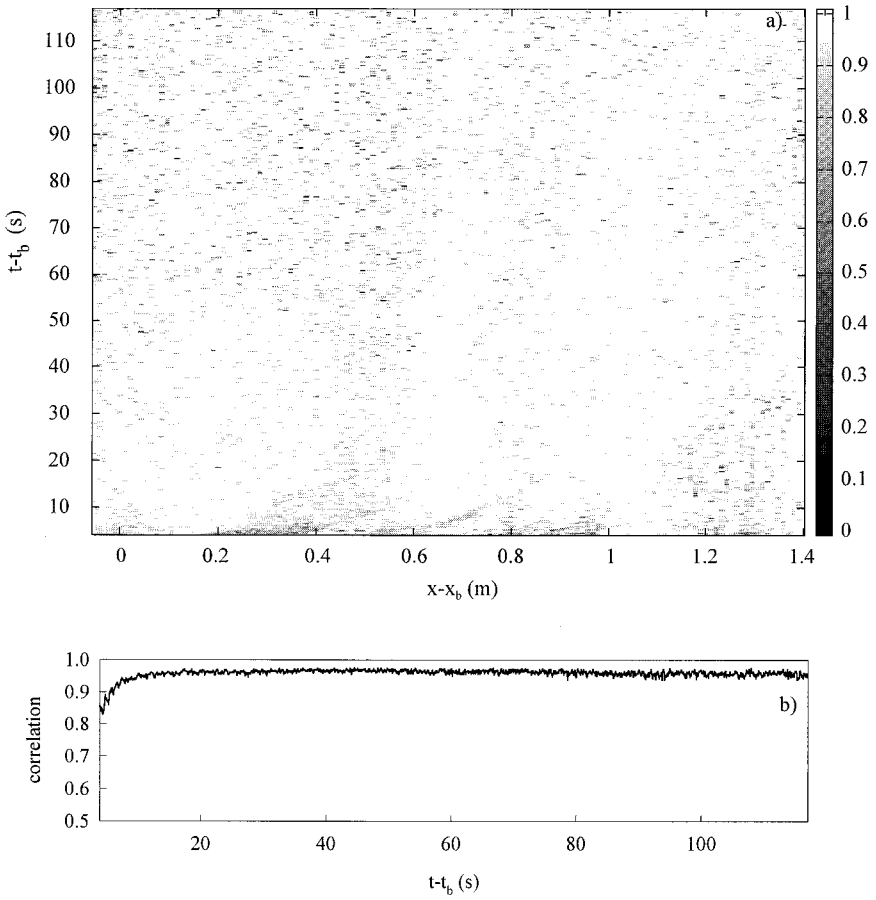

FIG. 6. (a) Correlation field corresponding to the data of Fig. 4a. (b) Time series of the correlation coefficient averaged over the profile. The overall correlation coefficient for the event is 0.96.

expect the signal from the waves to disappear for wavenumbers around 30 rad m^{-1}, as observed in Fig. 4c. The other striking feature of the wavenumber–frequency spectrum is a low-frequency, broad wavenumber signal that is believed to be turbulence. Figure 4d shows a closer view.

Filtering out the signal in the neighborhood of the dispersion curve (i.e., removing the surface waves), and inverting this two-dimensional spectrum gives the velocity field dominated by the turbulence. To do this, we designed a smoothed 2D transfer function window, similar in size to the 2D spectrum. It is designed to have a 0% transmission coefficient for the signal around the surface wave dispersion curve, and a 100% transmission elsewhere. This filter corresponds to suppressing a V-shaped wedge with its tip at the origin and enclosing both negative and positive phase velocity waves. The filtering is performed in real space by convolving the velocity data with the inverse 2D spectrum of the filter window. Figure 4e is the result of filtering the data from Fig. 4a. A direct comparison of the two images confirms that this simple filtering successfully removed most of the surface waves while leaving the turbulence. It is clear from Fig. 4c that such a strategy will be successful, except perhaps in the low wavenumber/low-frequency regime. For example, Fig. 4e still shows some vestiges of the seiche.

It is now possible to use common statistical tools to analyze the turbulence created by the breaker (Tennekes and Lumley 1972). We consider the one-dimensional wavenumber spectrum defined as

$$\Phi(k, t) = \frac{1}{2\pi} \int_{-\infty}^{+\infty} R(r, t) e^{-ikr}\, dr, \tag{13}$$

where $R(r,t)$ is the longitudinal spatial correlation given by

$$R(r, t) = \langle u_1(x_1, t) u_1(x_1 + r, t) \rangle. \tag{14}$$

The angle brackets denote spatial averaging and $u_1(x_1, t)$ is the along-beam component of the velocity. The wavenumber spectrum defined by Eq. (13) is normalized such that[1]

[1] Parseval's theorem is satisfied over positive wavenumbers only.

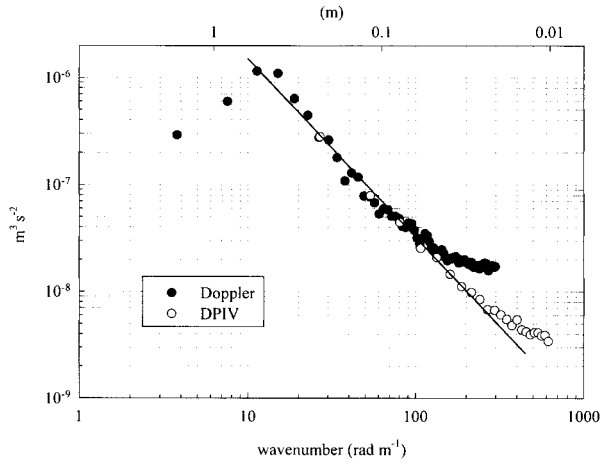

FIG. 7. Wavenumber spectra computed from the data of Figs. 4b and 4e. The solid line has a $-5/3$ slope.

$$\int_0^\infty \Phi(k, t)\, dk = \langle u_1(x_1, t)^2 \rangle. \tag{15}$$

From the data of Fig. 4e it is possible to construct a wavenumber spectrogram of the velocity field, by taking the spectrum in the range direction only. Such a process gives the evolution in time of the wavenumber spectrum for individual profiles. Figure 4f shows the spectrogram corresponding to the data of Fig. 4e, where spectra of individual profiles are averaged over 1 s (15 profiles). Figure 4f exhibits several features. There is a maximum of energy around 12 rad m^{-1} as well as ''bursts'' that propagate to higher wavenumber (smaller scales) with time. It is not clear, however, if this is the effect of advection of eddies through the beam of the profiler, a transfer of energy to smaller scales through the classical ''energy cascade,'' or both. Note also that the main peak near 12 rad m^{-1} breaks up around $t - t_b = 50$ s, the time at which the dominant ''eddy'' in Fig. 4e slows down and disperses.

Averaging the spectrograms, $\Phi(k, t)$, in time from individual profiles gives a single wavenumber spectrum $\Phi(k)$ for each breaking event. It is then possible to compare spectra given by both the DPIV and the Dopbeam. For the common 54 s of data, the wavenumber spectra are calculated as described above. The results of this process are presented in Fig. 7 and show wavenumber spectra of the data presented in Figs. 4e and 4b. The DPIV data are not filtered prior to the calculation of the wavenumber spectra. As mentioned earlier in the description of Fig. 4c, because of the measurement depth and the exponential decay of orbital velocity with depth, the wave signal is apparent only for wavenumbers lower than 30 rad m^{-1}. Now, due to the limited length of the field of view (23 cm), the wavenumber spectrum from a DPIV profile will have a resolution of 27 rad m^{-1} and will not be contaminated by waves (except perhaps for the lowest spectral estimate). In summary, long waves compared to the profile length will not significantly affect the spectrum, and short waves that would have a noticeable effect over a profile are too short to penetrate down to the measurement depth. Figure 7 demonstrates that over the common range of wavenumbers very good agreement is achieved. As expected, because of its longer range, the Dopbeam extends to lower wavenumbers, and, with its finer resolution, the DPIV extends to higher wavenumbers.

3) INSTRUMENT NOISE

Figure 7 shows a rather surprising flattening of the Doppler wavenumber spectrum at approximately 160 rad m^{-1}. In fact, wavenumber spectra of still water data (taken in the same conditions as the experiment, but when no wave packet is sent), and calculated as described above, yield a flat distribution of energy at a level of 3.10^{-9} m^3 s^{-2} across the wavenumber domain. This noise level is entirely consistent with the expected velocity error of 1.6 mm s^{-1}. So, instead of an intersection with the noise floor, the flattening of the wavenumber spectrum is most likely due to spatial aliasing. This will be affected by both spatial smearing due to the averaging down to 15 Hz, and also by the shape of the sampling volume. It is interesting to note that at a range of 1 m, the half-power beamwidth is 3.5 cm, or 175 rad m^{-1}. The likelihood that this flattening is not the noise floor of the instrument will also be emphasized in the next section where we show that the wavenumber spectra scale uniformly across the wavenumber domain for different wave energy levels.

4) KINETIC ENERGY DISSIPATION

The wavenumber spectra for the Dopbeam data were then calculated for the three wave cases mentioned in section 3b. The results are plotted in Fig. 8. Each spectrum corresponds to a particular wave slope and is the ensemble average of a single wavenumber spectrum (similar to that of Fig. 7) over eight repeats of the experiment. Single wavenumber spectra were obtained as described above, by averaging the wavenumber spectrogram of each event up to $t - t_b = 60$ s. The error bars are the standard deviation of the spectral estimate over the ensemble of eight events. The peaks of the spectrum, as expected, shift to slightly lower wavenumbers with increasing breaker strength, denoting the increasing size of the energy containing eddies with breaker scale. Also, the spectra exhibit an approximate $-5/3$ slope, as indicated by the solid line. This region of constant slope in the spectra is believed to be the inertial subrange for which the one-dimensional wavenumber spectrum takes the form (Hinze 1975)

$$\Phi(k) = \frac{18}{55}\left(\frac{8\varepsilon}{9\alpha}\right)^{2/3} k^{-5/3}, \tag{16}$$

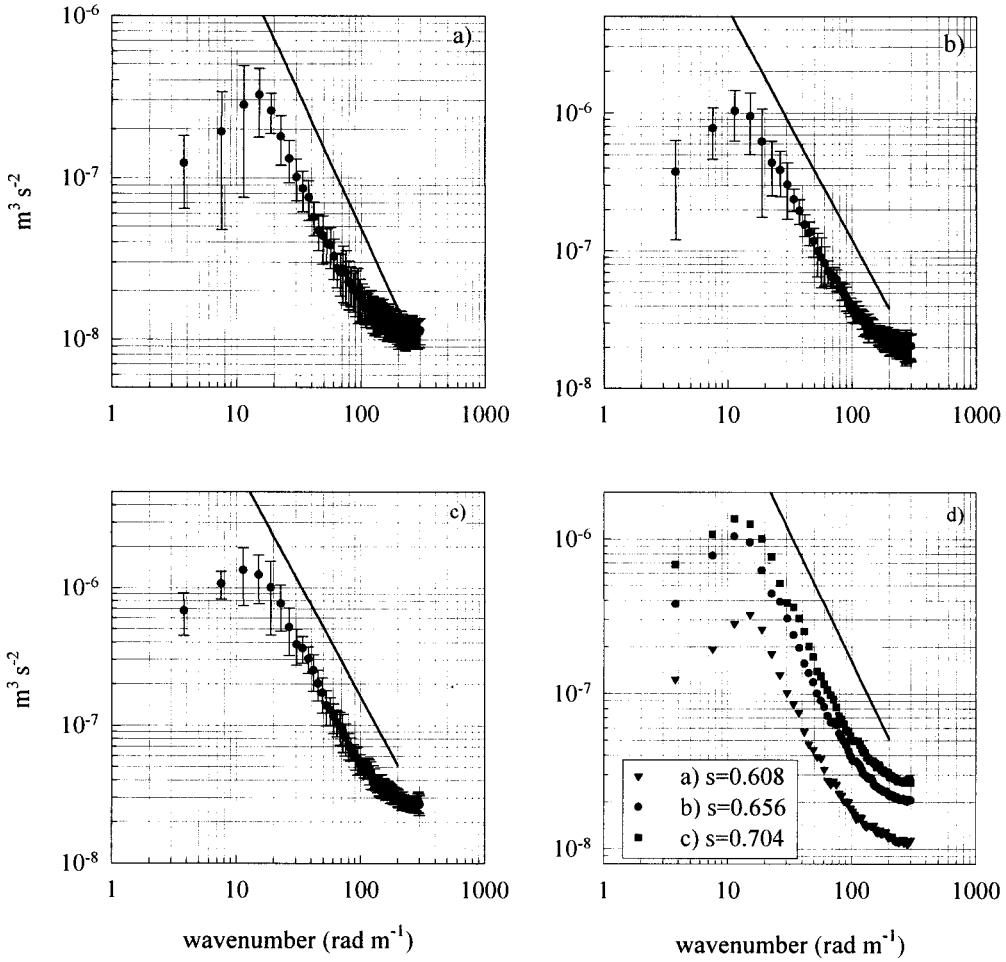

FIG. 8. Wavenumber spectra for the three waves cases: (a) $S = 0.608$, (b) $S = 0.656$, and (c) $S = 0.704$. The error bars are the standard deviation of the spectral estimates over the ensemble (of eight repeats for each breaker case). The solid line is the $-5/3$ spectral slope. (d) Relative spectral levels for the three breaker cases.

where α is Heisenberg's constant ($\alpha \approx 0.4$ for high Reynolds number flows). This simple relationship between wavenumber spectrum and dissipation rate can be used to determine ε by fitting a $k^{-5/3}$ constant slope curve through the inertial subrange part of the spectrum. We have done so, and the fitting of a $k^{-5/3}$ curve has been applied to the data between 20 and 80 rad m^{-1}. Note here that with a noise floor of approximately 3.10^{-9} $m^3 s^{-2}$, the minimum kinetic energy dissipation that can be detected is on the order of 10^{-8} $m^2 s^{-3}$. Also, if the flow were locally isotropic, the dissipation rate could be expressed as

$$\varepsilon = \langle 15\nu \overline{\left(\frac{\partial u_1(x_1, t)}{\partial x_1}\right)^2} \rangle. \quad (17)$$

This gives an alternative way of calculating ε. An estimate of the shear was obtained via a first-order bin-to-bin finite difference on the velocity profile. The double average is taken over the same data required to compute the wavenumber spectra (i.e., the entire profile and up to $t - t_b = 60$ s). Table 1 shows the results for ε calculated both from the spectra and the velocity fields using Eqs. (16) and (17). These results show an increasing discrepancy between estimates of ε using Eqs. (16) or (17) as S increases. This is believed to be due to the fact that our along-beam spatial resolution is limited to 1.05 cm, making it impossible to fully resolve the higher wavenumbers and the dissipation range, especially in the more energetic breakers. In that case Eq. (17) would lead to an underestimate of ε (with an increasing error as the energy increases and the inertial range cutoff moves to higher wavenumbers), whereas

TABLE 1. Kinetic energy dissipation estimates.

Wave slope	ϵ ($m^2 s^{-3}$) [from Eq. (16)]	ϵ ($m^2 s^{-3}$) [from Eq. (17)]
$S = 0.608$	4.22×10^{-7}	4.12×10^{-7}
$S = 0.656$	1.85×10^{-6}	1.07×10^{-6}
$S = 0.704$	3.43×10^{-6}	2.04×10^{-6}

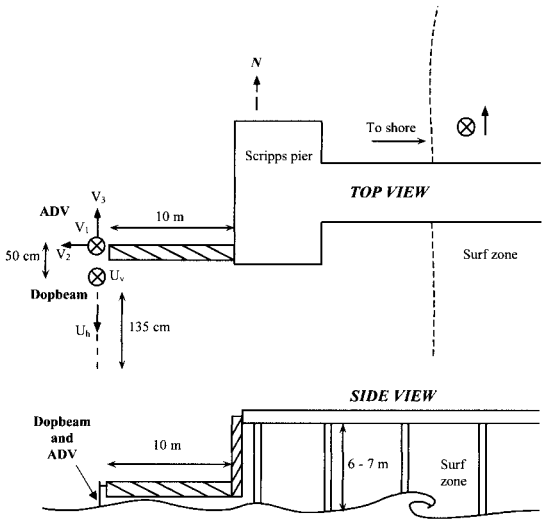

FIG. 9. Experimental setup on the pier at Scripps Institution of Oceanography (not to scale).

Eq. (16) only relies on the spectral levels in the resolved inertial subrange.

4. Field measurements

a. Experimental setup

Some preliminary experiments were conducted from Scripps pier, both seaward and shoreward of the breaker zone. The data taken outside the breaker zone were collected for two different orientations of the transducer: horizontally parallel to shore and vertically downward. This allowed us to collect horizontal $U_h(r, t)$ and vertical $U_v(r, t)$ velocity profiles, where r is range and t is time. The Dopbeam was attached to a rigid mount at the end of a 10-m-long boom fixed seaward off Scripps pier (Fig. 9). In the horizontal position, the transducer was placed at a depth of 40–50 cm from the mean water level, whereas in the vertical position, it was placed at a smaller depth so that the first useful bin would be at a depth of 40–50 cm. A single-point acoustic probe was used to take simultaneous velocity measurements [acoustic Doppler velocimeter (ADV); Sontek, San Diego, California]. However, to avoid flow interference, the ADV was mounted facing the opposite direction to the Dopbeam and at a distance of 50 cm from the Dopbeam transducer. The ADV is capable of measuring three components of the velocity (V_1, V_2, and V_3, which are oriented as shown in Fig. 9). A pressure and velocity sensor was deployed 30 m north of the pier for measurements of wave height and currents. Also, air and water temperature are available from the Scripps pier weather station. Additional environmental parameters, including wind speed, wind direction, and wave height, were also recorded using an anemometer and a directional wire wave gauge array.

The Dopbeam was set to ping with a 555-Hz repetition rate giving a 12 cm s^{-1} velocity ambiguity and a maximum range of 1.35 m. Averaging of the velocity profiles led to a sampling frequency of 15 profiles per second, the same as in the laboratory. Simultaneous measurements with the ADV were achieved through appropriate triggering at a similar sampling frequency.

TABLE 2. Environmental conditions for the two days presented.

Date	Water temperature (°C)	Air temperature (°C)	Wind speed (m s^{-1})	Significant wave height (m)
29 Mar 1997	18	15	6.7	0.7
9 Apr 1997	17	15	10.3	1.8

b. Results

The results presented here are taken from two different days that illustrate different wind and wave conditions (Table 2). The first day (29 March 1997), was a relatively calm day with low wind speed and a very weak swell, whereas 9 April 1997 was considerably rougher with significant whitecap coverage and small-scale breaking occurring outside the surf zone. Figure 10 shows photographs of the setup for these two days. Note in Fig. 10b the small-scale breakers and whitecaps.

Figure 11a is a typical example of the alongshore velocity profile data recorded by the Dopbeam on 28 March 1997. The horizontal axis is time and the vertical axis gives the range from the transducer in centimeters. In the data presented here, the useful velocity range of the instrument has been extended, when necessary, beyond the ambiguity velocity by unwrapping the phase in both space and time. It is possible to automatically identify ''jumps'' in the velocity records corresponding to jumps from $-\pi$ to π (or vice versa) of Ψ [see Eq. (1)]. Once identified, the erroneous phase is replaced by its appropriate modulo-2π value. This may lead to a doubling or tripling of the useful velocity range. Other techniques including pulse coding may also be used to enhance the velocity range.

When mounted horizontally alongshore, most of the orbital velocity of the long waves is orthogonal to the beam, and the predominant signal is from the wind waves and the turbulence. Although the profile was taken parallel to shore to minimize any velocity component from the swell, it is clear from Fig. 11a that wind waves with shorter period are present and dominate much of the velocity record. Note that for deep water waves the orbital velocity decays exponentially with depth so that only waves with a wavelength of approximately 80 cm and longer will have an effect at that depth. Therefore, even though the orbital velocities from those shorter waves are apparent over almost the total length of the profile, they will be present only (if at all) in the low wavenumber region of the spectrum, leaving the inertial subrange unaffected. When the transducer is mounted vertically, the dominant signal is from the vertical com-

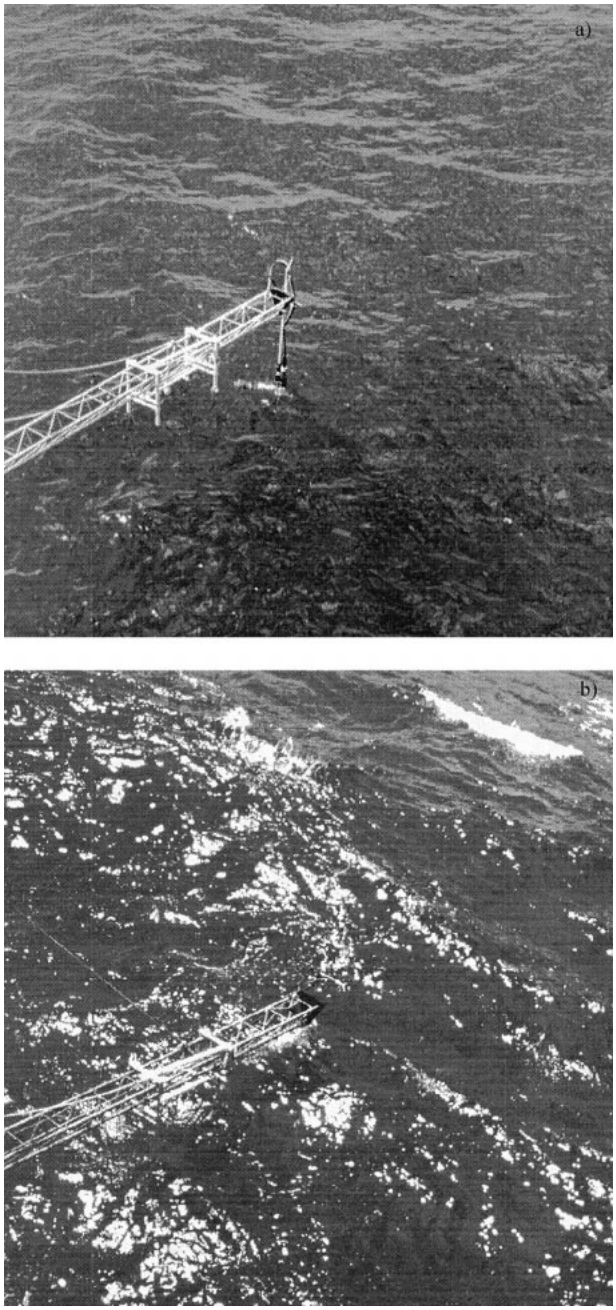

FIG. 10. Photographs of the pier setup for (a) 28 Mar 1997 and (b) 9 Apr 1997.

ponent of the orbital velocity, which for these long waves is nearly constant along the range of the Dopbeam, and therefore hardly contributes to the spectrum. Thus, in both cases, much of the orbital motion of the waves is filtered out. This is the tremendous advantage of spatial (wavenumber) measurements over single-point measurements. Along with removing most of the surface waves from the data by an optimum orientation of the instrument, further digital filtering was used. Since the velocity signal due to the waves is nearly constant along the range, much less than one wavelength is contained in each profile, which makes it impossible to extract the dispersion relationship for the waves, as was done in the laboratory. However, the fact that the motion induced by the waves is nearly constant along the profile allows us to linearly detrend each profile, thus ensuring that the bulk of the variance along the range of the instrument (and consequently the wavenumber spectrum) is dominated by turbulence.

The correlation field corresponding to the velocity field presented in Fig. 11a has an overall average of $\overline{\overline{C}} = 0.88$ and shows very few signatures of decorrelation due to surface waves advecting scatters across the acoustic beam. Natural scatters such as plankton, suspended particles, microbubbles, or density microstructure (see Plueddemann and Pinkel 1989; Goodman 1990; He and Hay 1993) appear to be sufficient to ensure good backscatter levels. Also, comparison with the ADV is very good. For this particular case V_3 is the component of the velocity measured by the ADV that is aligned with the profile. Simultaneous velocity time series of V_3 and U_h (at a range of 20 cm), although not strictly coincident,[2] agree very well (Figs. 12a and 12b). Moreover, Fig. 12c shows spectra of the ADV velocities as well as a range-averaged spectrum of the velocities taken with the Dopbeam. The agreement is very good. The spectra from the Dopbeam and from the V_3-component spectrum compare well up to about 3 Hz. We do not expect agreement at high frequency since the sampling points are not coincident. Frequency spectra for V_1, V_2, and V_3 are shown for reference. The peak at about 1.2 Hz is not observed in the V_2 or V_3 directions, nor in the wave gauge data. We conclude that it is most likely due to horizontal vibrations of the boom. Again, such vibrations will result in a uniform error in the range velocity measured by the Dopbeam and thus will not contaminate the velocity variance or wavenumber spectrum along the profile. Figure 12d shows frequency spectra for one single horizontal velocity bin (depth = 55 cm) and two vertical velocities bins (depth = 55 cm, 110 cm) recorded the same day by the Dopbeam. The absence of the peak at 1.2 Hz in both spectra for U_v supports the interpretation that this feature is most likely due to horizontal motion of the boom.

In a similar manner to that used to measure wavenumber spectra for a breaking event in the laboratory, we compute wavenumber spectra for the velocity profile taken in the field by averaging individual spectra of profiles for approximately 40 s. The resulting spectra are plotted in Fig. 13. They exhibit an approximate $-5/3$ slope. From Fig. 13 it is obvious that, as expected, the energy levels are higher for 9 April 1997. We note that the spectral slope appears to be slightly steeper than

[2] The Dopbeam and ADV are separated by 0.5 m and U_h is taken 20 cm from the Dopbeam. This results in a total separation of 70 cm between the two measurement points.

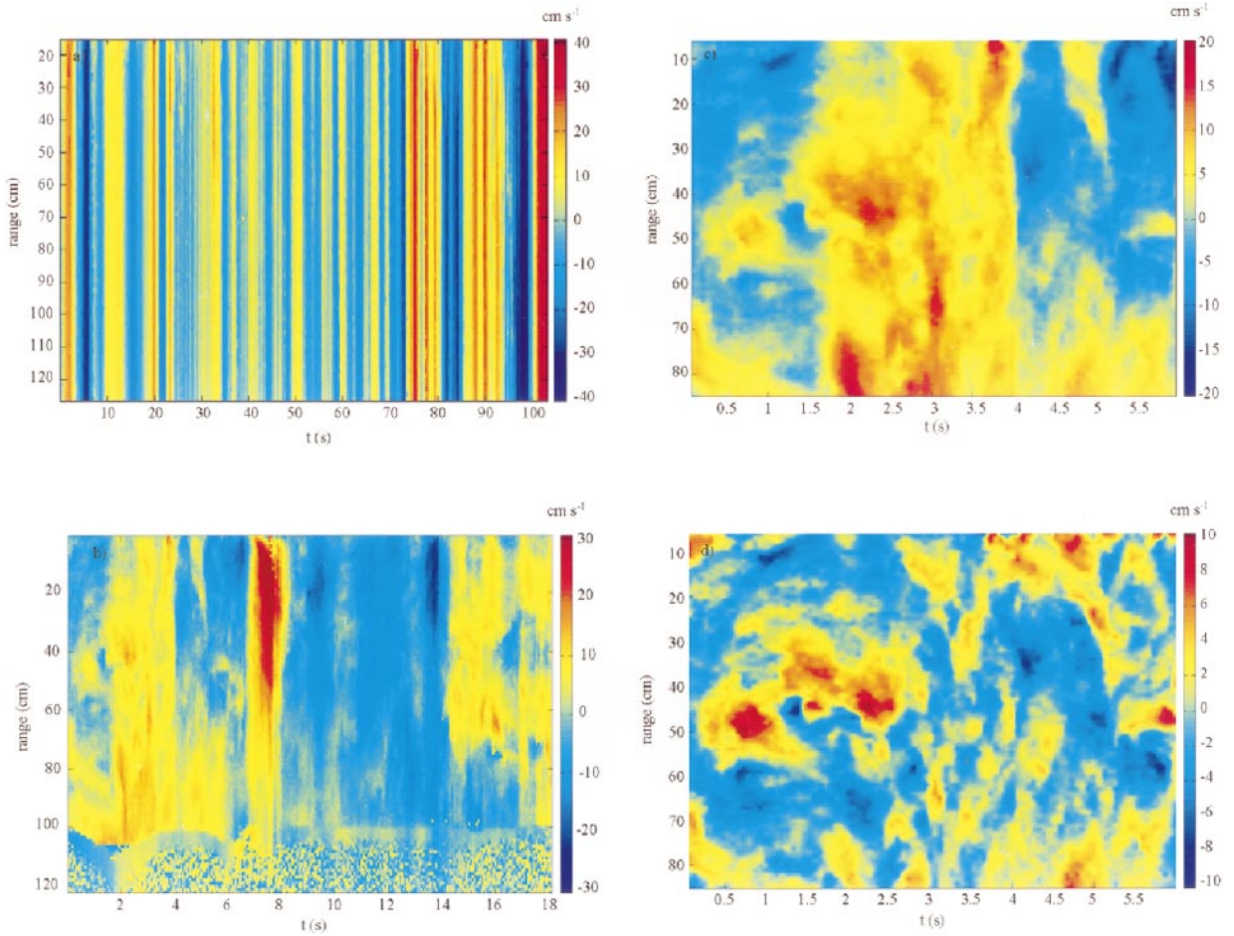

FIG. 11. (a) Example of the horizontal alongshore velocity $U_h(r, t)$ recorded by the Dopbeam on 28 Mar 1997. (b) Example of the vertical velocity recorded by the Dopbeam in the surf zone. Note that the bottom is apparent at a range of approximately 1 m. (c) Example of the vertical velocity in the surf zone; close-up of the data from (b). (d) Vertical velocity in the surf zone from (c) where each profile has been linearly detrended. Note the structures and size distribution of the turbulent eddies.

$-5/3$ for the most energetic day. It is also interesting to note that the energy contained in a vertical profile is less than the energy in the corresponding horizontal profile. This indicates that the variance of the velocity over a vertical profile is smaller, which may result from vertical decay of turbulence in a very shallow surface layer or anisotropy of the turbulence. This is discussed below.

c. Surf zone

Although it is not our intention to study surf zone processes, it is interesting to test the Dopbeam in a very energetic environment. To stay at an approximately constant depth of 40 cm, the Dopbeam was fixed to a float. Again both vertical (downward) and horizontal orientations of the transducer were tested. Figure 11b shows the vertical velocity field. Note that the bottom is apparent at a range of 1 m, giving a total water depth of approximately 140 cm. Only 18 s of data are shown here since the rest of the record was corrupted due to high velocities and screening of the pings by large concentrations of bubbles and suspended sand. Although the wavenumber spectra plotted in Fig. 14 show comparable levels for both orientations of the profiles, they display significant departures from a $-5/3$ slope. This may be due to the fact that the turbulence in the breaker zone is statistically unsteady, nonuniform, and strongly intermittent so that the classical cascade, which leads to the inertial subrange does not have time to establish following each breaking event and during the relatively short sampling time. For the cases shown here the energy density at the lower wavenumbers is higher than expected for a classical inertial subrange. The surf zone data presented here show some remarkable features and demonstrate the ability of the Doppler sonar to directly measure turbulence velocities in the wavenumber domain. For example we have isolated and plotted in Fig. 11c the first 6 s of the data shown in Fig. 11b. A certain level of patchiness is already clearly apparent, but there is also a notable wave component to the velocity field. In fact, this wave component is likely due to the movement of the float and, consequently, the Dopbeam, rel-

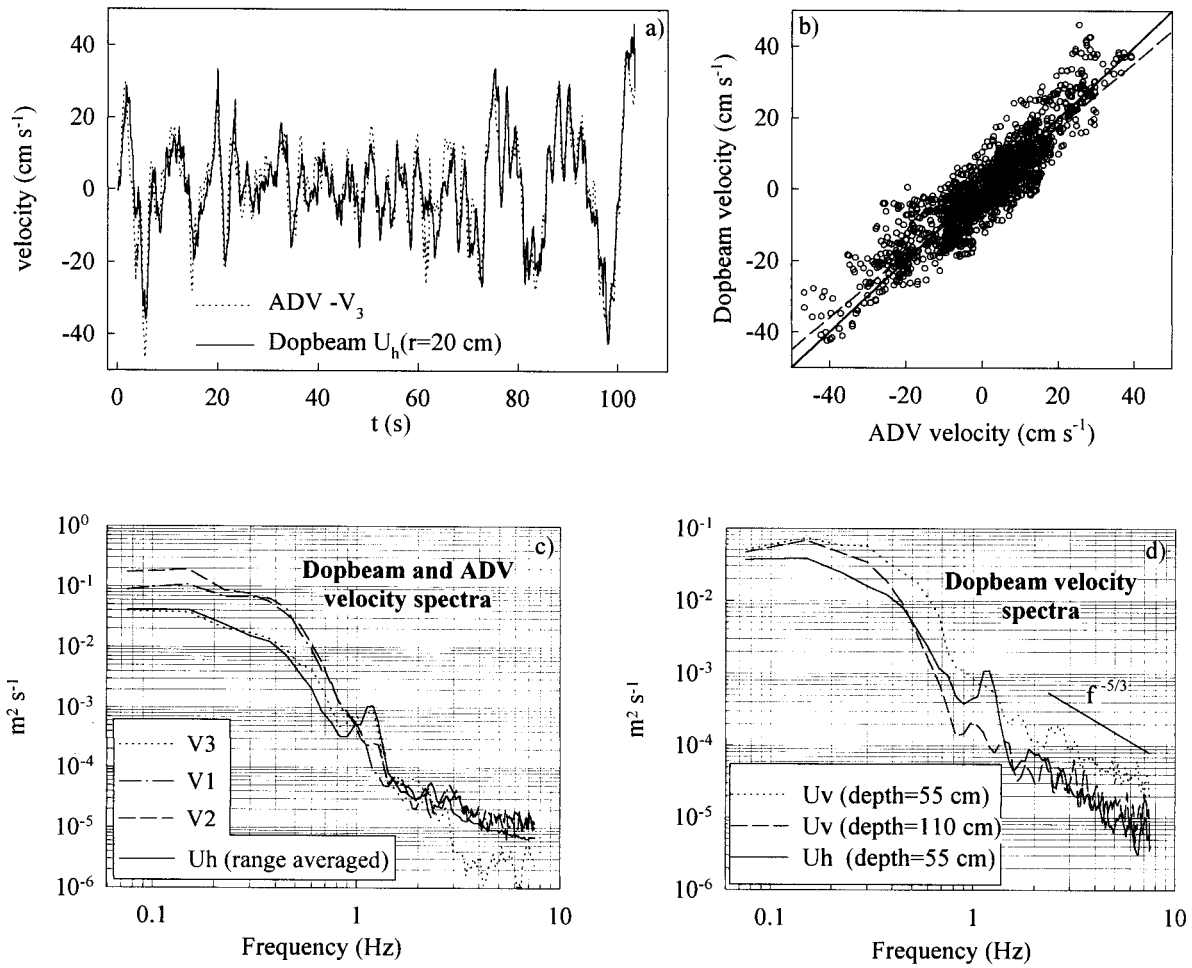

FIG. 12. (a) Time series of the ADV horizontal alongshore velocity $-V_3$ and the Doppler velocity U_h at a range of 20 cm (from the data of Fig. 11a). (b) Doppler velocity vs ADV velocity. The solid line has a slope of 1. The dashed line is the linear regression through the data (slope = 0.92). (c) Frequency spectra for the ADV velocities and range-averaged frequency spectra for the Dopbeam velocities. (d) Frequency spectra from single-point Doppler velocities.

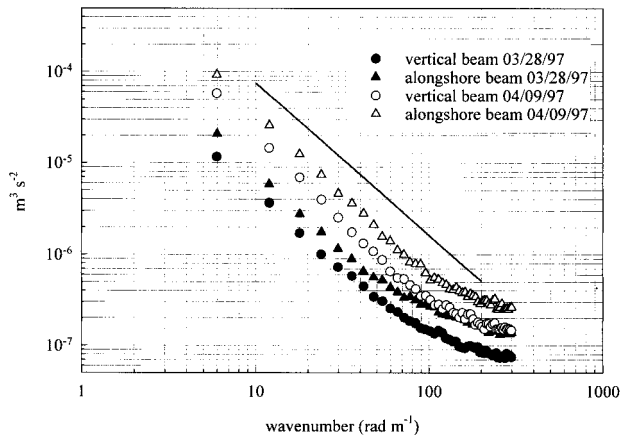

FIG. 13. Wavenumber spectra for both orientations of the Dopbeam for 28 Mar and 9 Apr 1997. The solid line has a $-5/3$ slope.

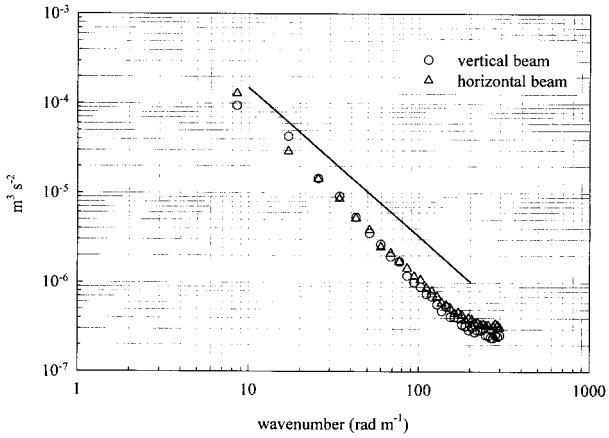

FIG. 14. Wavenumber spectra for both orientations of the Dopbeam in the surf zone. The solid line has a $-5/3$ slope.

ative to the water column. Note in Fig. 11b that between $t = 0$ s and $t = 2$ s, the Doppler moves away from the bottom, and between $t = 2$ s and $t = 4$ s, it moves toward the bottom. This movement generates an erroneous offset of the velocity profiles (negative at first and then positive). This shift affects the entire profile, but the relative bin-to-bin velocity is unaffected. Figure 11d is the data shown in Fig. 11c, where each profile has been linearly detrended (so that the mean velocity difference from profile to profile is minimal) and shows some remarkable structures with a wide range of scales. Figure 11d is just a snapshot over 6 s of the vertical turbulent velocity in the surf zone, and yet, as suspected, shows high levels of temporal and spatial intermittency.

5. Discussion

a. Time-dependent dissipation

In the laboratory, as mentioned before, the wavenumber spectrum $\Phi(k)$ associated with a single event, such as the one shown in Fig. 7, is a time average of the wavenumber spectrogram $\Phi(k, t)$ over 54 s. However, if the spectrum of a single profile $\Phi(k, t)$ behaves as $k^{-5/3}$, it is then possible to extract from Eq. (16) the kinetic energy dissipation as a function of time

$$\varepsilon(t) = \left(\frac{18}{55}\right)^{-3/2}\left(\frac{8}{9\alpha}\right)^{-1} k^{5/2}\Phi(k, t)^{3/2}. \qquad (18)$$

Still, a certain amount of averaging in time is necessary in order to obtain satisfactory convergence of $\Phi(k, t)$ toward a $-5/3$ slope. For example, with 1 s of time averaging the wavenumber spectra still show significant structure (see Fig. 4f). However, a 5-s average provides a satisfactory convergence of the spectral levels to a $-5/3$ slope, which then permits the calculation of $\varepsilon(t)$ according to Eq. (18). Similarly, based on Eq. (17), we can define the time-dependent dissipation as

$$\varepsilon(t) = \langle 15\nu\left(\frac{\partial u_1(x_1, t)}{\partial x_1}\right)^2\rangle. \qquad (19)$$

We have independently used these two methods to estimate the time evolution of the dissipation after a breaking event. Figure 15a shows the results of this process applied to the data of Fig. 4e. Equation (18) provides an estimate of ε every 5 s, and the result is plotted with open circles placed in the center of the 5-s bin. On the other hand, Eq. (19) gives an estimate of ε (plotted as dots) for every profile (at a 15-Hz rate). The two estimates agree quite well and show a very rapid decrease in the dissipation level after the breaker. This decrease is qualitatively consistent with the observations of Rapp and Melville (1990). Note, however, that they showed that 90% of the energy lost by the wave is dissipated in the first four wave periods, while the data shown here does not include this time period. In Fig. 15a, it is clear that [as mentioned in the comments of Table 1 in section 3C(2)] the error made by evaluating ε using Eq. (17) or (19) increases with increasing turbulence levels, as the dissipation range moves to higher (unresolved) wavenumbers. Figure 15b shows $\varepsilon(t)$ obtained with Eq. (19) for the three different wave slopes studied. Each point is an ensemble average over eight single realizations similar to the one shown in Fig. 15a. It appears that the dissipation behaves as $\varepsilon \propto t^{-n}$ with n in the range from -1 to -1.25. It is possible to go further in the estimation of the dissipation rate. From Eq. (17) we already defined Eq. (19), where the average of the squared shear is taken over space only. Similarly, we can define

$$\varepsilon(x, t_i) = 15\nu\overline{\left(\frac{\partial u_1(x_1, t)}{\partial x_1}\right)^2}, \qquad (20)$$

where the overbar denotes a 5-s average in time centered on t_i. This provides an estimate of a ''local'' (in space and time) $\varepsilon(x, t_i)$ with a spatial resolution of 1.05 cm (no averaging in space) and a time resolution of 5 s.

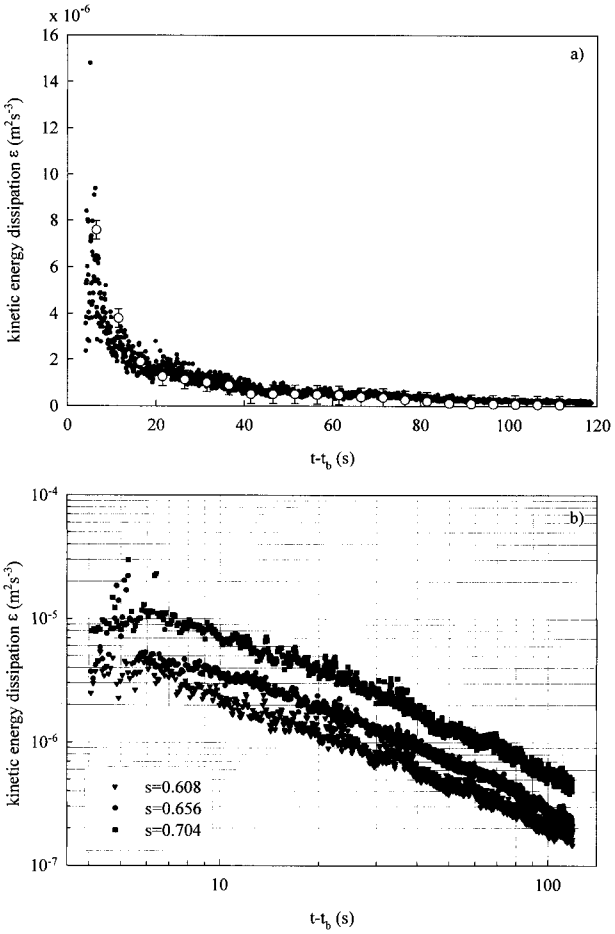

FIG. 15. (a) Estimate of the time-dependent kinetic energy dissipation $\varepsilon(t)$ using Eq. (18) = ○, and Eq. (19) = ● from the data of Fig. 4e. Note the extremely fast decay of the dissipation level after the breaking event. (b) Relative dissipation levels for the three breaker cases.

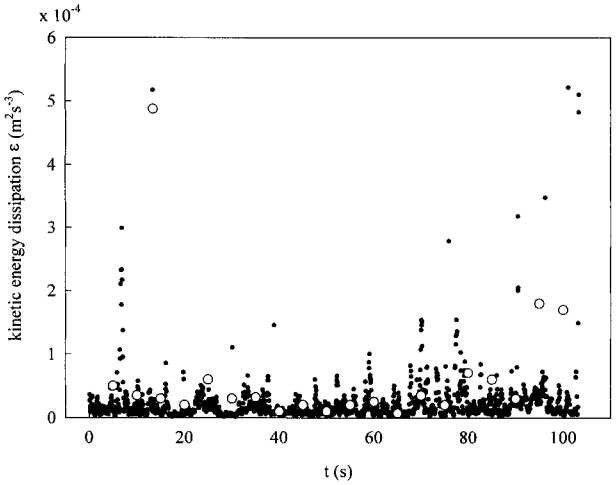

FIG. 16. Estimate of the time-dependent kinetic energy dissipation $\varepsilon(t)$ using Eq. (18) = ○, and Eq. (19) = ● from the data of Fig. 11a. Note the high degree of temporal intermittency in the dissipation levels. Both estimates show numerous and large (up to an order of magnitude) excursions above the background dissipation level.

The result is plotted in Fig. 4g and shows, as anticipated, large (although underestimated) values of the dissipation directly beneath the breaker. This result is to be taken qualitatively since we know that Eq. (20) probably underestimates ε. Nevertheless, it shows that turbulent kinetic energy is likely to be dissipated extremely quickly and intermittently beneath individual breakers. Note here that beneath the breaker, ε covers two to three orders of magnitude over the time of 2 min and a 1-m range.

Similar estimates to that of Fig. 15 can be made in the field. Figure 16 shows the time evolution of ε for the data of Fig. 11a obtained using Eqs. (18) and (19). Note here the significant temporal intermittency. In the short time presented in Fig. 16, both estimates show numerous and large excursions of the turbulent kinetic energy dissipation. These events are short and of approximately an order of magnitude in amplitude. Moreover, the extremely rapid decrease of the dissipation levels observed in the laboratory after a breaking event suggests that the ''ambient'' levels are probably at least one order of magnitude lower than those experienced immediately after a breaker. Once more, this emphasizes the difficulty of using profiling instruments to measure the dissipation in the upper boundary layer of the ocean and stresses the need for a nearly continuous sampling of the fluid velocities in order to more accurately measure the dissipation near the surface.

b. Taylor's hypothesis

One of the motivations of this work has been the need to develop direct spatial measurements of turbulence that avoid the use of Taylor's hypothesis. In a wavenumber-frequency spectrum, the presence of a linear feature passing through the origin would mean that it is possible to establish a one-to-one correspondence between wavenumber and frequency spectra, with the slope of the signal having the dimension of a velocity (an advection velocity V_T giving the desired relation between time and space). This transformation from wavenumber to frequency is the basis of Taylor's frozen field hypothesis. For example, it is possible to fit a line through the strong, quasi-linear signal near the origin of Fig. 4c. This signal is believed to be related to the main eddy apparent in Fig. 4a. Indeed, the velocity extracted from the linear fit is 0.013 m s^{-1} and is comparable to the apparent advection velocity of the eddy 0.011–0.016 m s^{-1} (see Fig. 4a). However, a closer inspection of the signal of the turbulence in Fig. 4d reveals that it is not strictly linear. The main vortex in Fig. 4a slows down and eventually breaks up into smaller vortices, leading to the creation of a broader range of length and time scales and consequently to a distortion of a possible linear relationship between wavenumber and frequency. This is observed in Fig. 4d where the slope of the wavenumber–frequency signal of the turbulence decreases with increasing wavenumbers. Thus, for a given frequency, there can be a number of local spectral peaks distributed along the wavenumber domain, or, for a given wavenumber, there can be multiple maxima at different frequencies. Therefore, it is unclear that Taylor's hypothesis would be directly applicable in the case of intermittent events, such as local overturning or surface breaking. Clearly, this issue needs to be addressed in further detail.

In the field, wavenumber spectra such as those shown in Fig. 13 exhibit a slope very close to the expected $-5/3$, while in the frequency domain the inertial subrange appears less clearly (see Fig. 12d). Obviously, this leads to uncertainties in the estimate of dissipation levels based on frequency spectra. One of the criteria for the use of Taylor's hypothesis is that the advection velocity V_T required for the frequency-wavenumber transformation be large compared to the turbulent velocities. Lumley and Terray (1983) extended this criterion to unsteady advection and have shown that for deep water gravity waves with a narrow directional distribution, V_T could be adequately replaced by the rms of the surface waves orbital velocity $U_{\text{rms}}^{\text{orb}}$. They found the frequency spectrum to be represented by

$$S(f) = \frac{7}{110} 2^{4/3} \Gamma\left(\frac{1}{3}\right) \left(\frac{8\varepsilon}{9\alpha} \frac{U_{\text{rms}}^{\text{orb}}}{2\pi}\right)^{2/3} f^{-5/3}, \qquad (21)$$

which is equivalent to Eq. (16) in the frequency domain. Nevertheless, the conditions over which the frequency–wavenumber transformation is valid greatly limits the range of usable data. In fact, we can expect that large orbital velocities correlate with high sea states, which in turn yield high turbulence levels. For example, for the data shown in Fig. 11a (and Fig. 12a) the rms of the orbital velocity is 11.6 cm s^{-1}, where the orbital velocity is the part of the velocity signal at frequencies below

0.75 Hz. The rms turbulent velocity is 1.63 cm s^{-1}, where the turbulent velocity is the velocity signal at frequencies above 2 Hz. If we consider the ratio of these rms velocities to be large enough, the use of Taylor's hypothesis allows the transformation of the frequency spectrum of the horizontal velocity U_h (Fig. 12d, solid line) into a wavenumber spectrum. However, this transformation would lead to an overestimation of the spectral level by a factor of approximately 2.5 when compared to the *measured* wavenumber spectrum (Fig. 13). Consequently, this would lead to an overestimate of the dissipation ε by about a factor of 4. From Eq. (21) and the frequency spectrum of U_h, we find $\varepsilon \approx 1.6 \times 10^{-4}$, whereas the wavenumber spectrum and the use of Eq. (16) give $\varepsilon \approx 4 \times 10^{-5}$.

Averaging the wavenumber spectra for horizontal and vertical profiles from Fig. 13 yields a single spectrum for given wind conditions. With Eq. (16), we can estimate the turbulent kinetic energy dissipation using the inertial subrange. This preliminary analysis gives ε $O(10^{-5})$ and $O(10^{-4})$ for 28 March 1997 and 9 April 1997, respectively. This compares favorably with Drennan et al. (1996), who give $\varepsilon \approx 2 \times 10^{-4}$ m^2 s^{-3} for a depth of 1.25 m and a wind speed of 12 m s^{-1}, or Anis and Moum (1995), who find $\varepsilon \approx 3 \times 10^{-4}$ m^2 s^{-3} for a depth of 1.5–5 m and a wind speed of 13 m s^{-1}. This also falls in the range of values measured by Terray et al. (1996). Furthermore, the friction velocity in water is given by $u_{*w}^2 = C_D \rho_a \rho_w^{-1} U_{10}^2$, where ρ_a is the density of air and U_{10} the wind speed at 10-m altitude, and if we consider an air–sea drag coefficient $C_D = O(10^{-3})$, then, for 28 March 1997 and 9 April 1997, we find a dimensionless value of the dissipation $\varepsilon \kappa z / u_{*w}^3$ of the order $O(5)$ and $O(14)$, respectively. This supports the recent measurements of a layer of enhanced dissipation near the surface of the ocean (Agrawal et al. 1992).

It is also interesting to examine in greater detail the difference between the spectral levels of vertical and horizontal motion. As mentioned before, Fig. 13 reveals that wavenumber spectra for vertical profiles (from 50-cm to approximately 140-cm depth) appear to be less energetic than those for horizontal profiles (at 50-cm depth). Is this because the turbulent motions are anisotropic, or because they are decaying with depth? Part of the answer is contained in Figs. 12c and 12d. In the low-frequency domain (<1 Hz) both the ADV and Dopbeam records show that the V_1 and V_2 directions contain more energy than the V_3 direction. This is not surprising since those directions are coplanar with the orbital motion of the main wave field. For higher frequencies, single-point measurements in the vertical direction at two different depths (Fig. 12d, dashed and dotted lines) suggest that the turbulence is weaker at greater depth. On the other hand, at a depth of 55 cm the frequency spectrum for the horizontal velocity U_h is lower than that for the vertical velocity U_v, indicating that perhaps the motion is anisotropic. Combined, these tendencies indicate that the increased power in the wavenumber spectrum associated with the horizontal profile is not due to an increased variance (in time) of the horizontal velocity, but is in fact due to an increased variance along the profile. Again, this emphasizes that Taylor's hypothesis must be used with caution. Here we find that the frequency spectrum for U_v is greater than for U_h, while the wavenumber spectrum of a vertical profile is lower than that of a horizontal profile, thereby eliminating the possibility of using a common V_T for both orientations.

It is noteworthy that in the surf zone dissipation estimates from the spectral level [Eq. (16)] compare well with previous estimates made by George et al. (1994). Using hot-film anemometers to measure time series of fluid velocity in the surf zone, they calculated frequency spectra of short ($\frac{1}{8}$ s) time records and projected each onto the wavenumber domain with the corresponding ''local'' mean velocity as an advection velocity V_T. We find $\varepsilon \approx O(10^{-3})$, while they give a lognormal distribution for ε centered on 0.4×10^{-3} m^2 s^{-3}. It is also to be noted that they observed spectral slopes ''flatter'' than the $-5/3$, with an average of -1.25, while our results tend toward slopes of -1.9. From Figs. 13 and 14, it appears that the more energetic the environment, the greater departure from the classical $-5/3$ we observe in the wavenumber spectra, and the steeper they appear to be. This seems to be consistent with turbulence intermittency models such as the β model (see Frish 1995).

Finally, we have shown that vibrations of the instrument leave wavenumber spectra unaffected to leading order, and any type of motion with a frequency less that the profiling rate ($\approx$500 Hz) will not modify the wavenumber spectra. This implies that an acoustic profiler such as the Dopbeam, while mounted on autonomous floating devices, may accurately measure wavenumber spectral levels in the field over a wide range of weather conditions.

6. Conclusions

We have presented tests of a 1.72-MHz, pulse-to-pulse, coherent acoustic Doppler profiler in both the laboratory and the field. The main advantage of the Dopbeam over conventional single-point velocity measurements is the ability to acquire profiles of the fluid velocity with a high sampling rate. The measurements yield two-dimensional data where the fluid velocity is a function of range and time. In the laboratory, direct comparisons of velocity and wavenumber spectra from the Dopbeam and DPIV measurements are very good. A two-dimensional Fourier transform of the data shows the fairly clear separation of the turbulence and the wave field, allowing for appropriate filtering. Spectrograms of the turbulence generated by breaking waves show the accelerating propagation of the spectral peak with time toward higher wavenumbers (i.e., the breakdown of energy containing eddies into smaller scales). Averaging

the wavenumber spectrogram of a breaking event over time yields a single wavenumber spectrum. Breaking waves of varying strength were studied and the spectra obtained exhibit a $-5/3$ spectral slope, the signature of an inertial subrange in the turbulence. Identifying the inertial subrange and measuring the spectral level permits direct estimates of the turbulent kinetic energy dissipation ε under breaking waves. In addition, the dissipation has been estimated using the variance of the shear along the velocity profiles collected by the Dopbeam. Both estimates were found to compare favorably. Finally, a qualitative estimate of local dissipation rate clearly shows that the turbulence is likely to be dissipated rapidly and locally under individual breakers.

In the field, velocity and frequency spectra comparisons with the ADV are good. Preliminary analysis of the data shows that the instrument can measure wavenumber spectra and resolve inertial subranges over wavelengths in the range $O(0.01–1$ m), demonstrating its usefulness for measuring turbulent dissipation in the upper mixed layer or surface-wave zone. Since any form of Taylor's hypothesis is avoided by the direct spatial measurement, the instrument is not limited to wave conditions that satisfy the requirements of a frequency–wavenumber transformation. Furthermore, vibrations or movement of the mounting platform of the instrument will be reflected along the entire profile and thus will not affect the measured spectral levels.

We conclude that the instrument may prove useful for direct field measurements of turbulent wavenumber spectra.

Acknowledgments. We wish to thank Dr. Len Zedel for numerous fruitful discussions and his help with the calibration of the Dopbeam. We are grateful to Eric Terrill, Mike Ritter, Chris White, and Anatol Rozenberg for their help with the measurements. We also wish to thank an anonymous reviewer whose comments helped clarify the text. We thank the organizers of the ONR-sponsored Microstructure Sensors Workshop, Mt. Hood, 1996, at which the majority of this work was first presented. This work was supported by NSF Grant OCE 95-05628.

REFERENCES

Agrawal, Y. C., E. A. Terray, M. A. Donelan, P. A. Hwang, A. J. Williams III, W. M. Drennan, K. K. Kahma, and S. A. Kitaigorodskii, 1992: Enhanced dissipation of kinetic energy beneath surface waves. *Nature,* **359,** 219–220.

Anis, A., and J. N. Moum, 1995: Surface wave–turbulence interactions: Scaling $\varepsilon(z)$ near the sea surface. *J. Phys. Oceanogr.,* **25,** 346–366.

Cabrera, R., K. Deines, B. Brumley, and E. Terray, 1987: Development of a practical coherent acoustic Doppler current profiler. *Proc. IEEE Fourth Working Conference on Current Measurement,* New York, NY, Institute of Electrical and Electronics Engineers, 93–97.

Craig, P. D., and M. L. Banner, 1994: Modeling wave-enhanced turbulence in the ocean surface layer. *J. Phys. Oceanogr.,* **24,** 2546–2559.

Drennan, W. M., K. K. Kahma, E. A. Terray, M. A. Donelan, and S. A. Kitaigorodskii, 1992: Observations of the enhancement of kinetic energy dissipation beneath breaking wind waves. *Breaking Waves: IUTAM Symposium Sydney, Autralia 1991,* M. L. Banner and R. H. L. Grimshaw, Eds., Springer-Verlag, 95–102.

——, M. A. Donelan, E. A. Terray, and K. B. Katsaros, 1996: Oceanic turbulence dissipation measurements in SWADE. *J. Phys. Oceanogr.,* **26,** 808–815.

Frish, U., 1995: *Turbulence.* Cambridge University Press, 296 pp.

Gargett, A. E., 1989: Ocean turbulence. *Annu. Rev. Fluid Mech.,* **21,** 419–451.

——, 1994: Observing turbulence with a modified acoustic Doppler current profiler. *J. Atmos. Oceanic Technol.,* **11,** 1592–1610.

George, R., R. E. Flick, and R. T. Guza, 1994: Observation of turbulence in the surf zone. *J. Geophys. Res.,* **99,** 801–810.

Goodman, L., 1990: Acoustic scattering from ocean microstructure. *J. Geophys. Res.,* **95,** 11 557–11 573.

Gregg, M. C., D. P. Winkel, and T. B. Sanford, 1993: Varieties of fully resolved spectra of vertical shear. *J. Phys. Oceanogr.,* **23,** 124–141.

Hay, A. E., 1991: Sound scattering from a particle-laden turbulent jet. *J. Acoust. Soc. Amer.,* **90,** 2055–2074.

He, C., and A. E. Hay, 1993: Broadband measurements of the acoustic backscatter cross section of sand particles in suspension. *J. Acoust. Soc. Amer.,* **94,** 2247–2254.

Hinze, J. O., 1975: *Turbulence.* McGraw-Hill, 790 pp.

Komen, G. J., M. Cavaleri, K. Hasselmann, S. Hasselmann, and P. A. E. M. Janssen, 1994: *Dynamics and Modelling of Ocean Waves.* Cambridge University Press, 532 pp.

Lhermitte, R., and R. Serafin, 1984: Pulse-to-pulse coherent Doppler signal processing techniques. *J. Atmos. Oceanic Technol.,* **1,** 293–308.

——, and U. Lemmin, 1990: Probing water turbulence by high frequency Doppler sonar. *Geophys. Res. Lett.,* **17,** 1549–1552.

——, and ——, 1994: Open-channel flow and turbulence measurement by high resolution Doppler sonar. *J. Atmos. Oceanic Technol.,* **11,** 1295–1308.

Loewen, M. R., and W. K. Melville, 1991: Microwave backscatter and acoustic radiation from breaking waves. *J. Fluid Mech.,* **224,** 601–623.

Lohrmann, A., B. Hackett, and L. P. Røed, 1990: High resolution measurements of turbulence, velocity and stress using a pulse-to-pulse coherent sonar. *J. Atmos. Oceanic Technol.,* **7,** 19–37.

Lumley, J. L., and E. A. Terray, 1983: Frequency spectra of frozen turbulence in a random wave field. *J. Phys. Oceanogr.,* **13,** 2000–2007.

McWilliams, J. C., P. P. Sullivan, and C.-H. Moeng, 1997: Langmuir turbulence in the ocean. *J. Fluid Mech.,* **334,** 1–30.

Melville, W. K., 1994: Energy dissipation by breaking waves. *J. Phys. Oceanogr.,* **24,** 2041–2049.

——, 1996: The role of surface-wave breaking in air–sea interaction. *Annu. Rev. Fluid Mech.,* **28,** 279–321.

——, R. Shear, and F. Veron, 1998: Laboratory measurements of the generation and evolution of Langmuir circulations. *J. Fluid Mech.,* **364,** 31–58.

Miller, K. S., and M. M. Rochwarger, 1972: A covariance approach to spectral moment estimation. *IEEE Trans. Info. Theory,* **18,** 588–596.

Oakey, N. S., and J. A. Elliot, 1982: Dissipation within the surface mixed layer. *J. Phys. Oceanogr.,* **12,** 171–185.

Osborn, T., D. M. Farmer, S. Vagle, S. A. Thorpe, and M. Cure, 1992: Measurements of bubble plumes and turbulence from a submarine. *Atmos.–Ocean,* **30,** 419–440.

Plueddemann, A. J., and R. Pinkel, 1989: Characterization of the patterns of diel migration using a Doppler sonar. *Deep-Sea Res.,* **36,** 509–530.

Rapp, R. J., and W. K. Melville, 1990: Laboratory measurements of

deep-water breaking waves. *Philos. Trans. Roy. Soc. London,* **331A,** 735–800.

Richard, S. D., A. D. Heathershaw, and P. D. Thorne, 1996: The effect of suspended particulate matter on sound attenuation in seawater. *J. Acoust. Soc. Amer.,* **100,** 1447–1450.

Siegel, D. A., and A. J. Plueddemann, 1991: The motion of a solid sphere in an oscillating flow: An evaluation of remotely sensed Doppler velocity estimates in the sea. *J. Atmos. Oceanic Technol.,* **8,** 296–304.

Skyllingstad, E. D., and D. W. Denbo, 1995: An ocean large-eddy simulation of Langmuir circulations and convection in the surface mixed layer. *J. Geophys. Res.,* **100,** 8501–8522.

Snyder, W. H., and J. L. Lumley, 1971: Some measurements of particle velocity autocorrelation functions in a turbulent flow. *J. Fluid Mech.,* **48,** 41–71.

Tennekes, H., and J. L. Lumley, 1972: *A First Course in Turbulence.* The MIT Press, 300 pp.

Terray, E. A., M. A. Donelan, Y. C. Agrawal, W. M. Drennan, K. K. Kahama, A. J. Williams III, P A. Hwang, and S. A. Kitaigorodskii, 1996: Estimates of kinetic energy dissipation under breaking waves. *J. Phys. Oceanogr.,* **26,** 792–807.

Terrill, E. J., 1998: Acoustic measurements of air entrainment by breaking waves. Ph.D. thesis, Scripps Institution of Oceanography, University of California, San Diego, 244 pp.

——, and W. K. Melville, 2000: A broadband acoustic technique for measurements of bubble size distributions: Laboratory and shallow water measurements. *J. Atmos. Oceanic Technol.,* in press.

Thorpe, S. A., 1993: Energy loss by breaking waves. *J. Phys. Oceanogr.,* **23,** 2498–2502.

Willert, C. E., and M. Gharib, 1991: Digital particle image velocimeter. *Expts. Fluids,* **10,** 181–193.

Zedel, L., A. E. Hays, R. Cabrera, and A. Lohrmann, 1996: Performance of a single-beam pule-to-pulse coherent Doppler profiler. *IEEE J. Ocean. Eng.,* **21,** 290–297.